Applied Catalysis B: Environmental 292 (2021) 120163

Contents lists available at ScienceDirect

Applied Catalysis B: Environmental

journal homepage: www.elsevier.com/locate/apcatb

# Cost-effective fast-synthesis of chabazite zeolites for the reduction of $NO_x$

Jingyan Zhang[a], Jian Liang[b], Honggen Peng[b,c,d,**], Yangyang Mi[b], Peng Luo[a], Hao Xu[a], Mingyuan He[a], Peng Wu[a,*]

[a] Shanghai Key Laboratory of Green Chemistry and Chemical Processes, Department of Chemistry and Molecular Engineering, East China Normal University, North Zhongshan Road 3663, 200062 Shanghai, China
[b] College of Chemistry, Nanchang University, 999 Xuefu Road, Nanchang, Jiangxi 330031, China
[c] Key Laboratory of Poyang Lake Environment and Resource Utilization, Ministry of Education, School of Resources Environmental and Chemical Engineering, Nanchang University, 999 Xuefu Road, Nanchang, Jiangxi 330031, China
[d] Guangdong Key Laboratory of Environmental Catalysis and Health Risk Control, School of Environmental Science and Engineering, Institute of Environmental Health and Pollution Control, Guangdong University of Technology, Guangzhou 510006, China

## ARTICLE INFO

*Keywords:*
CHA zeolites economization synthesis
Inter-zeolite conversion
Nitrogen oxides
Selective catalytic reduction
*de*$NO_x$

## ABSTRACT

The costly synthesis of conventional CHA zeolites for ammonia selective catalytic reduction of nitrogen oxides ($NH_3$-SCR of $NO_x$) has hindered their widespread applications. In this study, highly crystalline CHA zeolites (CHA-Y and CHA-B) were successfully synthesized from low-cost NaY and Al-rich beta precursors and alternately low cost or low content structure directing agents through the inter-zeolite conversion route. After ion exchange with Cu, the Cu−CHA-Y and Cu−CHA-B showed superior performance in the $NH_3$-SCR of $NO_x$ reaction, which can be attributed to their high surface area, abundant acidic sites. The *in situ* analysis by diffuse reflectance infrared Fourier transform spectroscopy (DRIFTS) revealed the reaction intermediates of $NH_3$-SCR of $NO_x$ over the low-cost prepared Cu−CHA catalysts. The as- prepared low-cost Cu−CHA catalysts are promising candidates for the reduction of $NO_x$ conforming to the economic production of *de*$NO_x$ catalysts.

## 1. Introduction

Nitrogen oxides ($NO_x$) is one of the major atmospheric pollutant gas emitted from vehicle engines and industrial boilers processes [1,2]. The hazards of $NO_x$ include formation of photochemical smog, acid rain, atmospheric haze and ozone. However, at present, the control of $NO_x$ emission remains a challenging task [3–6]. Thus, it is necessary to install an after-treatment system on the sources of harmful gases in order to effectively protect the environment. Various technologies have been developed and used in the after-treatment system. Commercial selective catalytic reduction of $NO_x$ by $NH_3$ ($NH_3$-SCR of $NO_x$) is the most efficient technology for $NO_x$ removal, and has been applied in exhaust purification systems for vehicles and industrial boilers [1,2,7]. Recently, much attention has been paid to ion-exchanged zeolites with active species (*e.g.*, Fe, Co, and Cu) [3,8–11], due to their uniform channels, abundant acidic sites, superior thermal and hydrothermal stability, and large surface area. Among them, Cu-exchanged small pore zeolites (SSZ-39, SSZ-13 and high-silica LTA) show good catalytic performance in $NH_3$-SCR of $NO_x$ [8,9,12]. Compared with Cu-SSZ-13, although Cu-SSZ-39 and Cu-LTA have good catalytic performance, especially in high temperature region, the organic template used in the synthesis process is more complicated, which limits their wide application. Recently, Cu-exchanged SSZ-13 with chabazite (CHA) structure has been commercialized for diesel vehicle emission control. The CHA topological structure consists of large cavities (8.35 Å × 8.35 Å × 8.23 Å) and eight-membered ring (8MR) pore windows (3.8 Å × 3.8 Å). Importantly, this structure plays an important beneficial role in providing better resistance to $SO_2$ [13]. In addition, the silicon-aluminum ratio (SAR) of zeolite is also a key factor influencing its hydrothermal and thermal stability. A SAR of 6–30 for CHA zeolite is considered stable after hydrothermal aging at 800 °C for 12 h [14]. In short, the proper topology and SAR play crucial roles in $NO_x$ removal. Although the small pore Cu-SSZ-13 zeolite with CHA crystal structure has been commercialized for diesel emission control system [15], its costly synthesis, to a large extent, limits its wide application. This is largely due to, as is widely known that numerous expensive organic template agents are usually necessary to synthesize CHA-type zeolites.

In the last few decades, many methods have been used to reduce the

---

* Corresponding author.
** Corresponding author at: College of Chemistry, Nanchang University, 999 Xuefu Road, Nanchang, Jiangxi 330031, China.
*E-mail addresses:* penghonggen@ncu.edu.cn (H. Peng), pwu@chem.ecnu.edu.cn (P. Wu).

https://doi.org/10.1016/j.apcatb.2021.120163
Received 9 December 2020; Received in revised form 26 February 2021; Accepted 16 March 2021

cost of synthesizing CHA zeolites [16–19], such as organic template free method [20], the method with minimal organic template [17], and the method replacing expensive templates with relatively inexpensive templates [16,18]. Additionally, Xiao et al. showed that the Cu-SSZ-13 zeolite can be produced by using an inexpensive copper-amine complex as template [19]. Wang et al. found that the SSZ-13 zeolite can be obtained by using a mixture of organic structure-directing agents (OSDA) composed of N, N, N-trimethyl -1-ammonium adamantine hydroxide (TMAdaOH) and the less expensive tetramethylammonium hydroxide (TMAOH) [16]. The mixture of TMAdaOH and TMAOH was used as structure directing agents to obtain the CHA structure, thereby effectively reducing the consumption of the more expensive TMAdaOH template. Inter-zeolite conversion technologies have also been developed. Corma et al. showed that the CHA-type zeolites can be synthesized by using high silica USY zeolites as precursor [18]. Recently, Jhung et al. demonstrated that SSZ-13 can also be obtained by using the high-silica beta zeolite as the precursor in the presence of a small amount of TMAdaOH ($TMAdaOH/SiO_2 \approx 0.03$) [17].

Even though the above strategies can to some extent reduce the cost of synthesizing CHA-type zeolites, considering the cost of USY and high-silica beta, the synthesis strategy of CHA-type zeolites by hydrothermal conversion of USY and high-silica beta did not have the noticeable advantage at the economic level. Therefore, reducing the cost and obtaining an acceptable zeolite precursor is still a difficult task. Fortunately, NaY ($SAR \approx 2.6$) and Al-rich beta ($SAR \approx 4.0$) can be prepared in the absence any organic templates [20]. However, the low-silica precursor as a source of silicon and aluminum is not adequate for the preparation of CHA zeolites for the $NH_3$-SCR of $NO_x$ reaction, due to the unstability of the low-silica CHA zeolites during practical application.

In this study, the high-silica precursors were synthesized by post-treating the low-cost NaY and Al-rich beta zeolites and using them in the synthesis of CHA-type zeolites for $NH_3$-SCR of $NO_x$. In particular, the high-silica CDY-wash-X precursor was obtained by treating NaY with aluminum sulfate and nitric acid, while, the high-silica H-beta-A precursor was also obtained by calcinating the Al-rich beta and treating it with nitric acid. Noteworthy, the Cu−CHA-Y and Cu−CHA-B, which were successfully synthesized through the hydrothermal conversion of the precursors CDY-wash-X and H-beta-A, exhibited superior selective catalytic reduction of $NO_x$ (*de*$NO_x$) performance. The structural and textural properties, redox behaviors, and other physicochemical properties of the catalysts were also investigated by various characterization methods. The *de*$NO_x$ reaction mechanism of the low-cost synthesis of Cu−CHA catalysts was determined by *in situ* diffuse reflectance infrared Fourier transform spectroscopy (DRIFTS).

## 2. Experimental section

### 2.1. Precursor preparation

Preparation of the low-cost high-silica CDY-wash-X precursor. A commercial NaY ($SAR \approx 2.6$) zeolite was used as raw material. The preparation of the CDY-wash-X precursor involves several steps, as depicted in Scheme 1.

Preparation of high silica H-beta-A precursor. The parent beta was prepared by using fumed silica, sodium hydroxide, and sodium aluminate as precursors, according to the method reported by Xiao et al. [20]. The preparation of the H-beta-A precursor is depicted in Scheme 2.

The detailed synthesis processes of the above two low-cost zeolite precursors are described in the Supporting Information.

### 2.2. CHA-type zeolite preparation

Synthesis of H−CHA-Y zeolite. The CHA-Y zeolite was synthesized by the hydrothermal conversion of the CDY-wash-X precursor under the guidance of the low-cost structure-directing agent tetraethylammonium hydroxide (TEAOH; 25 % aq. solution), as previously described by Corma et al., with some slight modifications [18]. The composition of the gel mixture was as follows: 1 $SiO_2$: 0.3 TEAOH: 0.08 $Na_2O$: 0.065 $Al_2O_3$: 15 $H_2O$.

Synthesis of H−CHA-B zeolite. The CHA-B zeolite was prepared by the hydrothermal conversion of H-beta-A under the guidance of TMAdaOH (25 % aq. solution), according to previously reported procedures with slight modifications [17]. The composition of the gel mixture was as follows: 1 $SiO_2$: 0.026 TMAdaOH: 0.077 $Na_2O$: 0.1 $K_2O$: 0.038 $Al_2O_3$: 36 $H_2O$.

Synthesis of traditional H-SSZ-13. For comparison, the traditional SSZ-13 was also synthesized by using colloidal silica, NaOH, $NaAlO_2$, and TMAdaOH as precursor. The synthesis process was similar to that in a previous report [12].

H−CHA-Y and H−CHA-B zeolites were obtained after 12 h crystallization. The detailed synthesis process of the above three H-type CHA zeolites is described in the Supporting Information.

### 2.3. Catalyst preparation

The Cu−CHA-Y (Cu−CHA-B or Cu-SSZ-13) catalysts were prepared by the exchange impregnation method. The process was similar to that in a previous report [21]. The Cu content was about 2 wt% and further confirmed by inductively coupled plasma-atomic emission spectroscopy (ICP-AES) analysis and the results are shown in **Table S1**. To determine the hydrothermal stability of the catalysts, these CHA-type zeolites were treated at 750 °C with 5 vol.% water vapor for 16 h, and designated as Cu−CHA-Y-HTA (Cu−CHA-B-HTA or Cu−SSZ-13-HTA).

### 2.4. Catalysts characterization

The physicochemical properties and reaction mechanisms of the samples were characterized by powder X-ray diffraction (PXRD) analysis, $^{29}Si$ and $^{27}Al$ MAS NMR spectra, $N_2$ adsorption/desorption technique, UV–vis spectroscopy, electron paramagnetic resonance (EPR) experiments, temperature-programmed reduction of hydrogen ($H_2$-TPR), scanning electron microscopy (SEM), scanning transmission electron microscopy mapping (STEM)-mapping analysis, $NH_3$ temperature programmed-desorption ($NH_3$-TPD), the pyridine adsorption FTIR spectra, X-ray photoelectron spectroscopy (XPS) and *in situ* DRIFTS. The detailed descriptions of these measuring methods are provided in the

**Scheme 1.** Dealumination process for low-cost NaY zeolite.

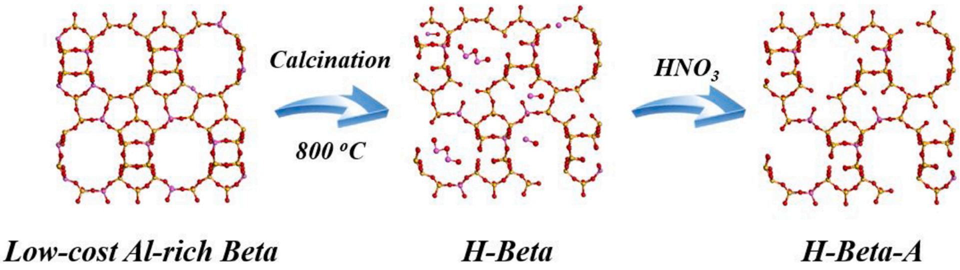

**Scheme 2.** Dealumination process for low-cost Al-rich Beta zeolite.

Supporting Information.

### 2.5. Catalytic performance evaluation

The catalysts for $NH_3$-SCR of $NO_x$ were evaluated using a fixed-bed quartz reactor (i.d. = 6 mm). Typically, 100 mg of the catalyst was loaded into a straight-type quartz tube. The feed consisted of 5% $O_2$, 500 ppm NO, 500 ppm $NH_3$, 5 vol% $H_2O$ with $N_2$ balance, and the total flow rate was set at 100 mL $min^{-1}$, which corresponds to the gas hourly space velocity (GHSV) was estimated to be ~48,000 $h^{-1}$. The dynamics test was conducted under 800,000 $h^{-1}$ with 5 vol% $H_2O$. The reaction temperature was monitored by placing a thermocouple on the catalyst bed with its head point touching the catalyst bed. All data were collected with increasing temperature. The reactants and products were measured by Fourier transform infrared (FT-IR) spectroscopy using a Nicolet Antaris IGS-Gas Analyzer (Thermo Fisher Scientific Inc., Waltham, MA, USA) equipped with a 2-m length gas cell. The NO conversion, $N_2$ selectivity and reaction rate were calculated using the following Eqs. (1), (2) and (3):

$$\text{NO Conversion } \% = \frac{(\mathrm{NO}+\mathrm{NO_2})_{\mathrm{inlet}} - (\mathrm{NO}+\mathrm{NO_2}+2\mathrm{N_2O})_{\mathrm{outlet}}}{(\mathrm{NO}+\mathrm{NO_2})_{\mathrm{inlet}}} \times 100\ [\%] \tag{1}$$

$$\mathrm{N_2}\text{ selectivity } = \left[1 - \frac{\mathrm{NO_2} + 2[\mathrm{N_2O}]_{\mathrm{outlet}}}{(\mathrm{NO_x})_{\mathrm{inlet}} + (\mathrm{NH_3})_{\mathrm{inlet}} - (\mathrm{NO_x})_{\mathrm{outlet}} - (\mathrm{NH_3})_{\mathrm{outlet}}}\right] \times 100[\%] \tag{2}$$

$$\text{Rate } \left[\mathrm{mol\ g_{cata}^{-1} s^{-1}}\right] = \frac{X_{\mathrm{NO_x}}\ [\%] \times F_{\mathrm{NO_x}}\ [\mathrm{L\ min^{-1}}]}{60\ [\mathrm{s\ min^{-1}}] \times 22.4\ [\mathrm{L\ mol^{-1}}] \times m_{\mathrm{cata}}[\mathrm{g}]} \tag{3}$$

where $X_{NOx}$ = $NO_x$ Conversion, [%], and $F_{NOx}$ = Flow rate of $NO_x$ [L ($NO_x$) $min^{-1}$].

## 3. Results and discussion

### 3.1. Crystal structure characterization of the precursor zeolites

The CDY-wash-X precursor zeolite was derived from the low-cost commercial NaY zeolite. The synthesis process was divided into three steps: (1) treatment of NaY with $Al_2(SO_4)_3$ to obtain the CDY zeolite; (2) washing the CDY zeolite with 0.08 M NaOH to obtain the CDY-wash; (3) further treatment of the CDY-wash with different concentrations of $HNO_3$ to obtain the CDY-wash-X. The SAR of NaY obtained after the above process can be increased from 2.6 to 7.7-11.4. CDY-wash-X, as initial silica-alumina source is considered feasible to obtain high-silica CHA and used for the $NH_3$-SCR of $NO_x$ reaction. The evolutionary process of the crystal structure and strength during above processes are shown in **Fig. S1(A)**. Besides the characteristic diffraction peaks of faujasite (FAU) zeolite, the other peaks at 18.1, 25.5, 30.2, 30.5, 40.6, and 48.0° are assigned to the typical diffractions of the Na alunite (PDF#41−1467) phase [22]. After treatment with NaOH, the alunite phase completely disappeared, while the crystallinity of the CDY-wash was not significantly changed. Additionally, the crystallinity of the CDY-wash-X zeolite exhibited a descending trend during the acid treatment process, especially for the CDY-wash-0.16. Fortunately, the CDY-wash-X zeolites still maintain the FAU topological structure.

The other low-cost precursor, H-beta-A, was derived from the low-cost Al-rich beta. The synthesis of the original Al-rich beta did not require any organic templates. The XRD patterns of the Na-beta, H-beta and H-beta-A are displayed in **Fig. S1 (B)**. The results indicated that the crystallinity of the beta zeolite has been well maintained during the dealumination process. The H-beta-A obtained by calcination at high temperature and acid treatment of Al-rich beta, not only had an increased SAR but also retained the crystal structure and strength. According to the above results, the two low-cost CDY-wash-X and H-beta-A precursors were successfully prepared.

### 3.2. Preparation and characterization of CHA-type zeolites

The CDY-wash-X was used as the initial silica-alumina source to obtain the CHA-Y through the hydrothermal conversion method. The results shown in Fig. 1 **(A–C)** reveal that all the CDY-wash-X precursor can be efficiently converted into the CHA-Y under the guidance of relatively low cost TEAOH as structure directing agent.

Although the crystal structure of the CDY-wash-X precursors had some damage, it is feasible to use them as initial silica-alumina sources. As it is widely known, the TEAOH plays a key role in the conversion process during the synthesis of the CHA zeolite [18]. It was found that the conversion of CDY-wash-X was incomplete or some other phases occurred (mordenite (MOR) or beta) during the inter-zeolite conversion process, when the concentration of TEAOH was too low. For example, the CDY-wash-0.14 used as the initial silica-alumina source could not be converted into the pure CHA-Y zeolite when the TEAOH to $SiO_2$ ratio was below 0.35. To reduce the cost of synthesizing the CHA-Y zeolite, the concentration of TEAOH was further optimized and the yield of CHA-Y zeolite was also calculated and the results listed in **Table S2**.

It is obvious that among all the CDY-wash-X precursors, CDY-wash-0.12 (SAR = 7.7) is the best option as the initial silica-alumina source to obtain the CHA-Y zeolite. It is also clearly seen that a highly pure CHA zeolite can be obtained even at a ratio of TEAOH to $SiO_2$ as low as 0.30. Additionally, we have been tracked the conversion process of CDY-wash-0.12 (**Fig. S2**). The FAU phase show a trend of firstly increasing and then decreasing, and CHA phase will gradually appear and eventually becomes the pure CHA phase from 0 to 12 h (**Fig. S2 (A)**). The increasing of FAU phase at 2 h, which was likely related to the dissolution of amorphous $SiO_2$ around the CDY-wash-0.12. **Fig. S2 (B)** shows the SEM images for CHA-Y zeolites synthesized by inter-zeolite conversion with different time. Apparently, there are very differences in the zeolite morphology and particle size as a function of conversion time. The surface features undergo an octahedral-to-spheroidal transformation in morphology. Simultaneously, the crystal size decreases from *ca.* 500 nm to 100 nm.

The H-beta-A precursor was obtained in the absence of any organic template. The preparation the of CHA-B zeolites from the H-beta-A

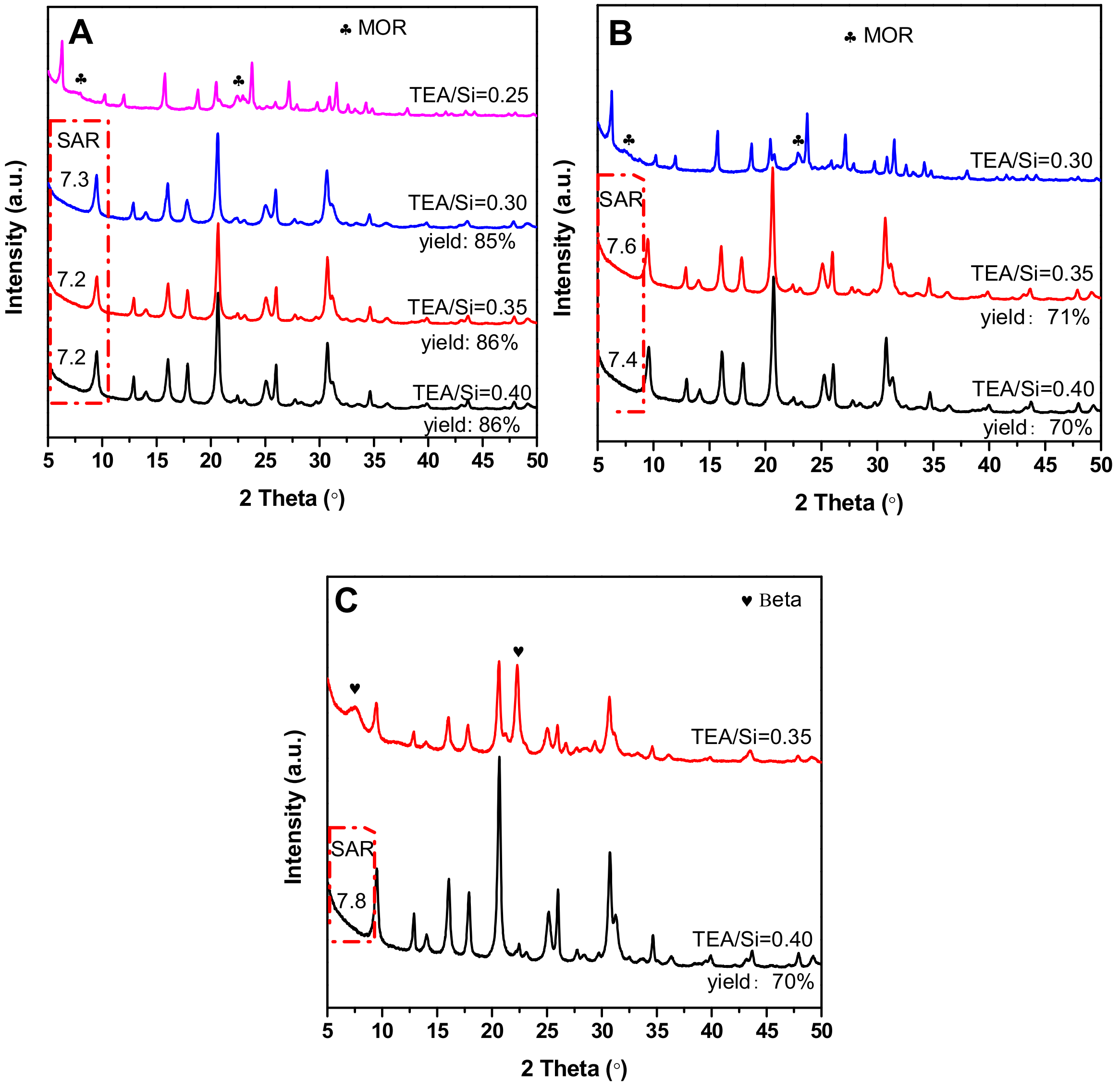

**Fig. 1.** XRD patterns. (A) CDY-wash-0.12 (SAR = 7.7), (B) CDY-wash-0.14 (SAR = 8.4) and (C) CDY-wash-0.16 (SAR = 11.4) as precursor respectively to synthetize CHA-Y with different TEAOH to $SiO_2$ ratios.

precursor was also optimized. Concretely, the results of the analysis of the effect of KOH, $H_2O$, TMAdaOH and seed content are separately shown in Fig. 2 **(A–D)**.

The MOR crystal phase was detected at low concentration of KOH, $H_2O$, TMAdaOH or seed. The optimal pure CHA-B zeolite was obtained when the molar composition of the starting gel was 1 $SiO_2$: 0.026 TMAdaOH: 0.077 $Na_2O$: 0.1 $K_2O$: 0.038 $Al_2O_3$: 36 $H_2O$: 2% seed. These results demonstrated that we can obtain high crystallinity CHA-B with the least TMAdaOH consumption ($TMAdaOH/SiO_2 = 0.026$), which effectively reduces the synthesis cost of CHA zeolites. Analogously, we also have tracked the conversion process of H-Beta-A (**Fig. S3**). After 2 h, the Beta phase almost completely disappeared and the CHA ($2\theta$ = *ca.* 9.4°, 30.8) produced, proving the growth of CHA phase was based on complete degradation of Beta. After only 4 h crystallinity, the pure CHA-B phase can be obtained (**Fig. S3 (A)**). **Fig. S2 (B)** shows the SEM images for CHA-B zeolites synthesized by inter-zeolite conversion with different time. Apparently, there are differences in the zeolite morphology and particle size as a function of conversion time. The surface features undergo an octahedral-to-cubic transformation in morphology. Simultaneously, the crystal size was increased from *ca.* 400 nm to 1.2 μm. Additionally, the morphology of CHA-B is similar to that of conventional SSZ-13 (**Fig. S4**). It can be anticipated that the difference in morphology is mainly due to the use of different organic templates. TEAOH and TMAdaOH show a tendency to produce nanometer- and micron- size zeolites, respectively. The results provided insights into the morphology control synthesis of CHA-type zeolites. Of note, the low-cost CHA-Y and CHA-B zeolites can be synthesized in only short time, which is faster than conventional SSZ-13.

### 3.2.1. *XRD analysis of Cu-exchanged catalysts*

The XRD patterns of H or Cu−CHA-Y, (CHA-B and SSZ-13) are displayed in Fig. 3 **(A)** and **Fig. S5 (A)**. The typical diffraction peaks are consistent with those of the CHA zeolite crystal [23]. The patterns of Cu−CHA-Y, (Cu−CHA-B and Cu-SSZ-13) catalysts are similar to those of the H- type supports.

In addition, the amplification curves (right side) showed that the diffraction peaks of CuO species was absent, and the peaks at 35.4 and 38.8° revealed that the Cu species was present in the ionic or cluster form. It should be noted that the crystal structure of all catalysts preserved the CHA framework well, even after the high-temperature hydrothermal aging process (at 750 °C, 16 h, 5% $H_2O$) (**Fig. S5 (B)**). The $^{27}$Al NMR and $^{29}$Si NMR spectra are displayed in Fig. 3 (B). From these

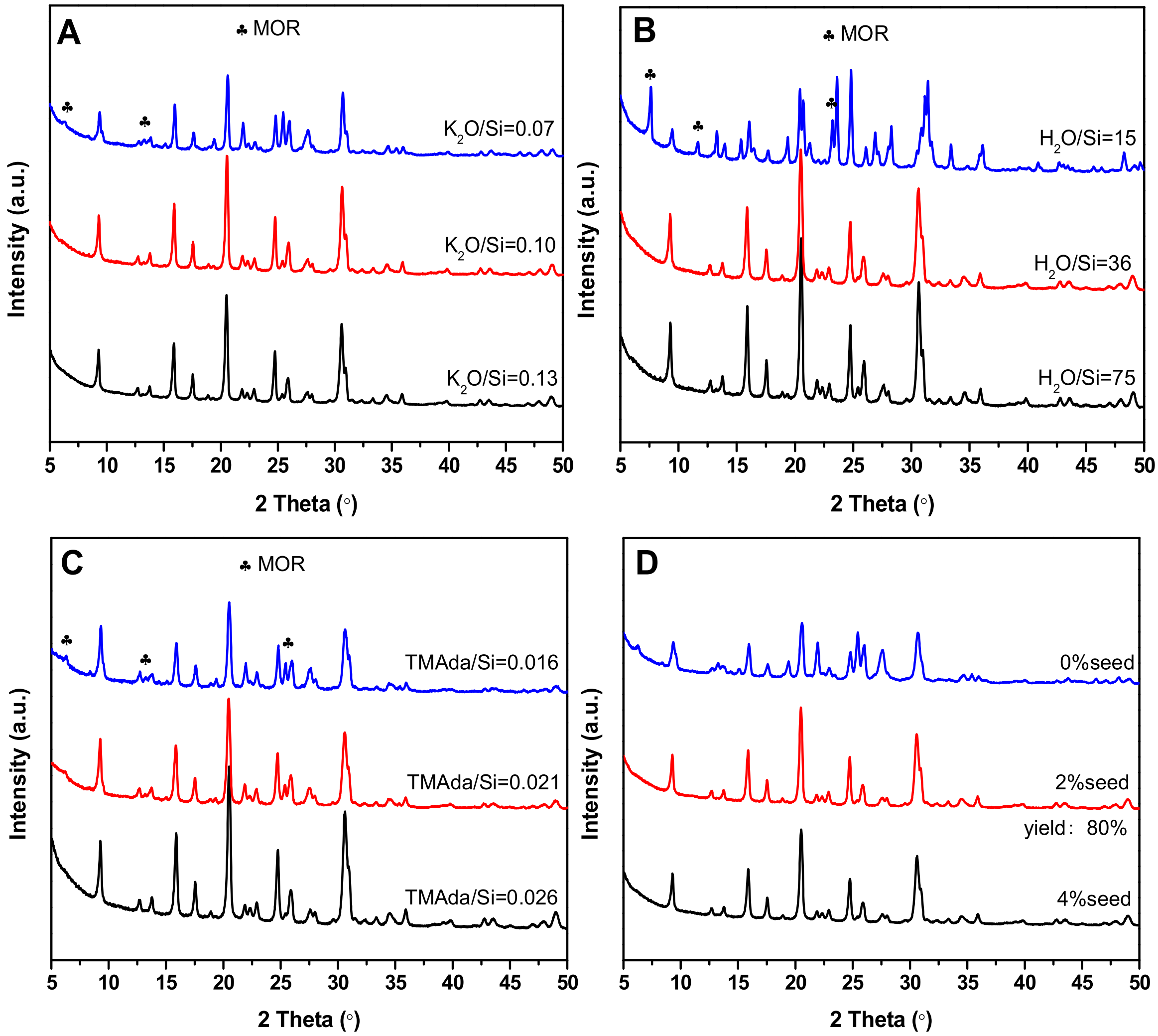

**Fig. 2.** XRD patterns. (A) Synthetize CHA-B with different $K_2O$ to $SiO_2$ ratios, (B) Synthetize CHA-B with different $H_2O$ to $SiO_2$ ratios, (C) Synthetize CHA-B with different TMAdaOH to $SiO_2$ ratios, (D) Synthetize CHA-B with different seed content.

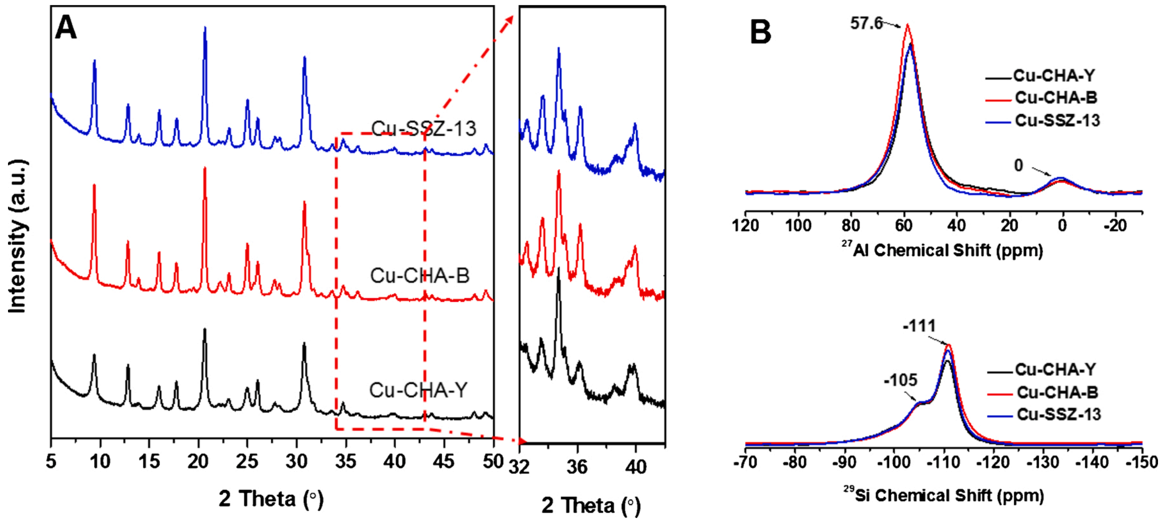

**Fig. 3.** (A) XRD patterns, and (B) $^{29}$Si, $^{27}$Al MAS NMR spectra of the Cu–CHA-Y, Cu–CHA-B and the conventional Cu-SSZ-13 catalysts.

spectra, we can see that tetrahedrally coordinated framework Al ($Al_F$) features as the major coordination environment were observed at about 57.6 ppm. The octahedrally coordinated extraframework Al (EFAl) with much smaller signals also observed at about 0 ppm [24,25]. As with the $^{27}$Al NMR data, $Al_F$ appears as the dominant species in all catalysts, which can provide a large number of acidic sites promoted $NH_3$

adsorption activation. All catalyst contains two framework tetrahedral Si features located at -111 and -105 ppm. The former was attributed to tetrahedral Si with four Si neighbors [Si(0Al, 4Si)] and the other was attributed to tetrahedral Si with three Si and one Al neighbors [Si(1Al, 3Si)] [12,26]. The profile area of band at -105 ppm is similar to each other. The profile area of band at -111 ppm sequence of the catalysts is in order of Cu−CHA-B **>** Cu-SSZ-13 **>** Cu−CHA-Y, consistent with SAR of catalysts, as determined by ICP results (Table S1).

To confirm the uniformity distribution of the Cu species on supports, all catalysts were further examined by STEM- mapping, and the images are shown in Fig. 4.

The Cu species distribute homogeneously with Al, Si and O elements, indicating that the Cu species are highly dispersed on the supports.

### 3.2.2. $N_2$ adsorption-desorption measurement

The $N_2$ adsorption-desorption method was used to further determine the textural properties of these as-prepared catalysts. The isotherms and the pore size distribution curves of the supports and catalysts are displayed in **Fig. S6**. Remarkably, H−CHA-Y and H−CHA-B exhibit a sharp increase in the relative pressure below 0.01, demonstrating the abundant presence of micropores [27]. Additionally, the H−CHA-Y exhibits a type IV isotherm in the relative pressure above 0.8, which may be due to the formation of mesopores [28].

Based on the results of the pore size distribution curves and SEM images (**Fig. S2**), we can conclude that the mesoporous structure is formed from stacks between crystal particles. The textural parameters of the supports and catalysts are listed in Table 1. Considering the small grain size of the H−CHA-Y zeolite, although it exhibits a slightly larger specific surface area and pore volume, we still think that none of the supports have undergone noticeable changes in textural properties. In other words, the textural properties of the H−CHA-Y and H−CHA-B zeolites are similar to those of the conventional H-SSZ-13 zeolite.

Compared with the supports, the addition of Cu species has a negligible effect on the surface area and pore volume, indicating that the Cu species are perfectly dispersed over the supports. Additionally, the catalysts after hydrothermal aging still retain larger surface areas and pore volumes, thus exhibiting high stability.

**Table 1**
The textural properties of various CHA-type zeolites.

| Samples | Specific surface area ($m^2$ $g^{-1}$)[a] | | | Pore volume ($cm^3$ $g^{-1}$)[b] | | |
|---|---|---|---|---|---|---|
| | $S_{BET}$ | $S_{micro}$ | $S_{ext}$ | $V_{tot}$ | $V_{micro}$ | $V_{meso}$ |
| H-CHA-Y | 562 | 484 | 78 | 0.64 | 0.38 | 0.26 |
| H-CHA-B | 527 | 500 | 27 | 0.33 | 0.22 | 0.11 |
| H-SSZ-13 | 541 | 514 | 27 | 0.36 | 0.24 | 0.12 |
| Cu-CHA-Y | 529 | 456 | 73 | 0.61 | 0.37 | 0.24 |
| Cu-CHA-B | 514 | 489 | 25 | 0.33 | 0.25 | 0.08 |
| Cu-SSZ-13 | 521 | 497 | 24 | 0.35 | 0.26 | 0.09 |
| Cu-CHA-Y-HTA | 480 | 416 | 64 | 0.59 | 0.39 | 0.20 |
| Cu-CHA-B-HTA | 485 | 470 | 15 | 0.30 | 0.22 | 0.08 |
| Cu-SSZ-13-HTA | 480 | 452 | 28 | 0.31 | 0.21 | 0.10 |

[a] Calculated by BET method.
[b] Determined by BJH method.

### 3.2.3. UV–vis spectroscopy study of the catalysts

The existing state of Cu species is a key factor to determine the *de*$NO_x$ performance. The UV–vis spectroscopy analysis was used to determine the existing state of Cu species on the catalysts, and the results are shown in Fig. 5 **(A)**. According to previous reports, there are four categories of Cu species, namely isolated $Cu^{2+}$, dimeric Cu/$CuO_x$ cluster, crystalline $CuO_x$, and bulk CuO [4]. The band at about 240 nm is attributed to the charge transfer of O → $Cu^{2+}$. The bands at ~ 310 and 380 nm hint to the presence of oligonuclear $[Cu\text{-}O\text{-}Cu]_n$ and crystalline $CuO_x$ species, respectively. Additionally, the band at ~ 780 nm is attributed to the $Cu^{2+}$ D-d transition. Clearly, the spectra of Cu−CHA-B is similar to that of Cu-SSZ-13, and isolated $Cu^{2+}$ is predominant among all the Cu species.

The isolated Cu ions stay exclusively at a +2 oxidation state under fully hydrated ambient conditions (*e.g.* $[Cu(OH)(H_2O)_5]^+$ and [Cu

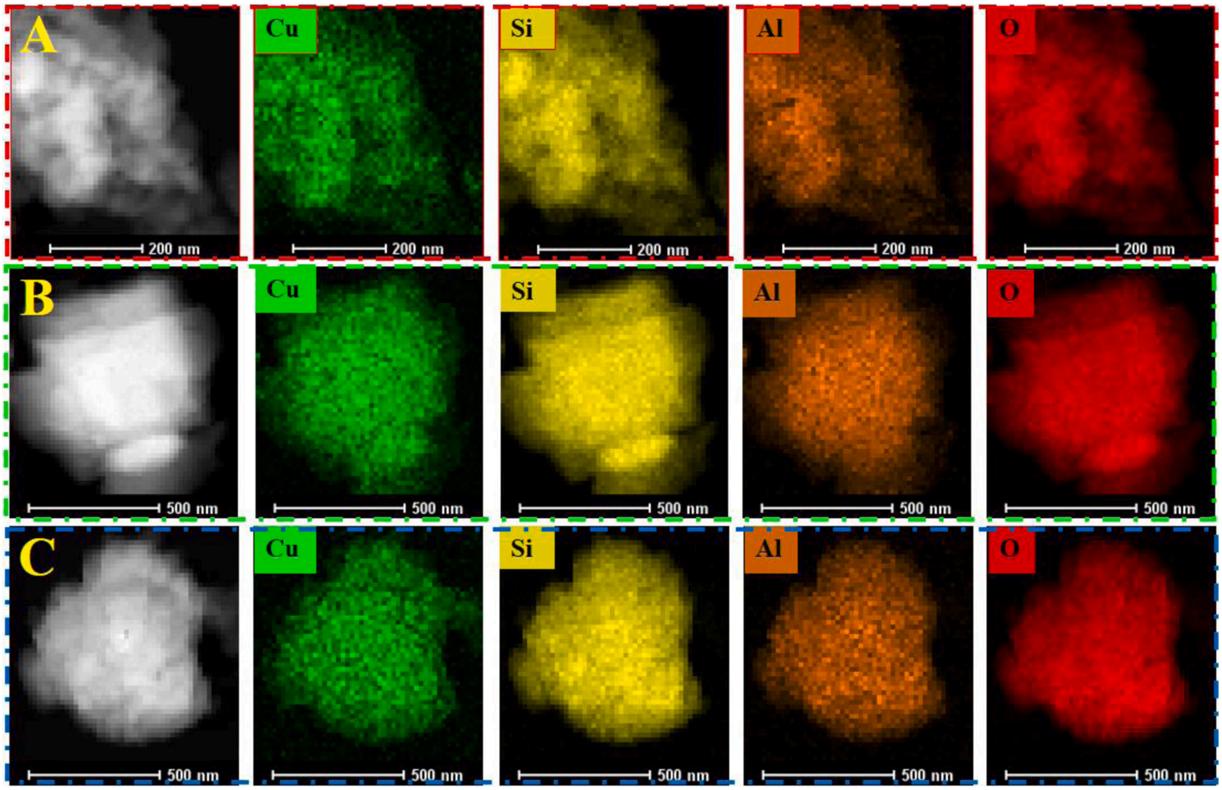

**Fig. 4.** STEM-mapping images: (A) Cu−CHA-Y, (B) Cu−CHA-B and (C) Cu-SSZ-13 catalysts.

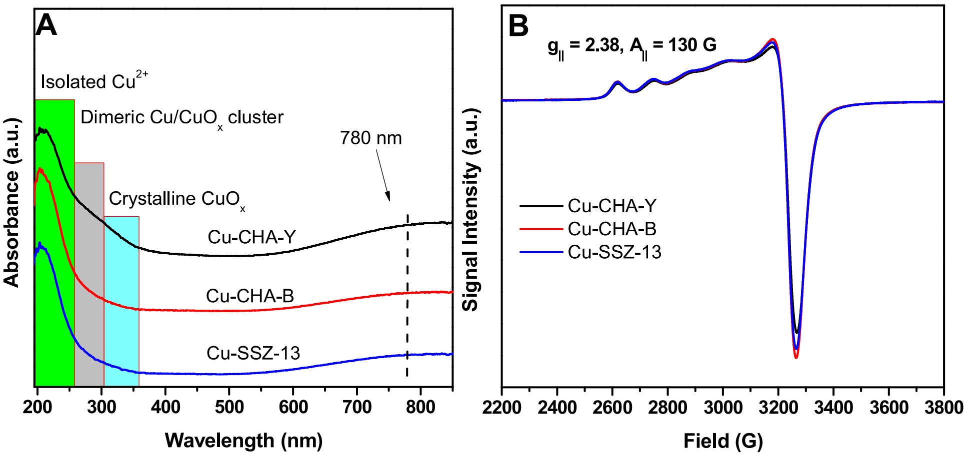

**Fig. 5.** (A) UV–vis spectroscopy of catalysts, (B) EPR spectra of hydrated catalysts measured at −118 °C.

$(H_2O)_6]^{2+}$ ions), and they are EPR active [29,30]. Therefore, amenable to quantitative interrogations *via* ERP. These Cu ions are quantified base on Cu-imide chelated standard solutions, and the results are listed in Table S1. Fig. 5 **(B)** shows EPR spectra for hydrated samples achieved at −118 °C. All signal lineshapes are very similar to each other. A single spectral feature is observed at high field. The hyperfine structures ($g_{||}$ = 2.38 and $A_{||}$ = 130 G) are resolved in the low field. These values are assigned to octahedral coordination of $Cu^{2+}$ ions [26,29]. It is worth noting that in all catalysts, this quantification sequence of isolated Cu ions is in order of Cu−CHA-B (2.0 wt %) > Cu-SSZ-13 (1.9 wt %) > Cu−CHA-Y (1.8 wt %), which matches total Cu loading quantification (2.0 wt %) by ICP results very well. The results proving that Cu in all catalysts are predominately EPR active $Cu^{2+}$ monomers, namely, isolated $Cu^{2+}$ is predominant among all the Cu species, which is beneficial for $NH_3$-SCR of $NO_x$.

### 3.2.4. Surface properties of the catalysts by XPS analysis

The XPS analysis was performed to further characterize the type of surface of the Cu species on the catalysts, and the results are displayed in **Fig. S7**. According to the reported literature and the characteristics of the XPS fingerprint, all spectra were deconvoluted in two categories, which were assigned to the different Cu species on the catalysts. The peaks at ~ 933.1 and 953.3 eV are attributed to the CuO species, and the other peaks at ~ 935.5 and 955.8 eV are assigned to isolated $Cu^{2+}$ species [31,32]. Moreover, additional satellite bands from 942.0 to 947.0 eV are present in the Cu 2p spectra, which are characteristic of the electronic configuration of unsaturated Cu on the Cu (II) component. Isolated $Cu^{2+}$ species acting as active centers play a significant key role in the $NH_3$-SCR of $NO_x$ reaction. The quantified data listed in **Table S1** demonstrated that compared with the Cu−CHA-Y, higher percentages of Cu species remain as isolated $Cu^{2+}$ in the Cu−CHA-B, which is in line with UV–vis spectroscopy analysis results.

### 3.2.5. $NH_3$-TPD analysis of the catalysts

The acidic sites of catalysts can adsorb and activate $NH_3$ molecules. Therefore, it also plays a crucial role in the $NH_3$-SCR of $NO_x$ reaction. Since a zeolite (Aluminosilicates) as a solid acid catalyst has abundant acidic sites, the $NH_3$-TPD technique was used to examine the acidic properties of these catalysts, and the deconvolution results are shown in Fig. 6 **(A).** The profile reveals a large amount of $NH_3$ desorption for all the three catalysts. For comparison purposes, the desorption peaks are categorized into three groups.

The α group is related to the physically adsorbed $NH_3$ species, the β group represents the $NH_3$ adsorbed on the Lewis acidic sites and weakly Brønsted acidic sites, and the γ group is associated with the $NH_3$ species captured by strong Brønsted acidic sites [33]. The quantified data presented in **Table S3** clearly shows that among all the three catalysts, Cu−CHA-Y has the largest number of acidic sites, which may be due to the high density of Al and larger specific surface area of the Cu−CHA-Y (details in **Table S1** and Table 1). Additionally, the content of acidic sites of Cu−CHA-B is similar to that of Cu-SSZ-13. In summary, Cu−CHA-Y and Cu−CHA-B have enough acidic sites to adsorb and activate $NH_3$

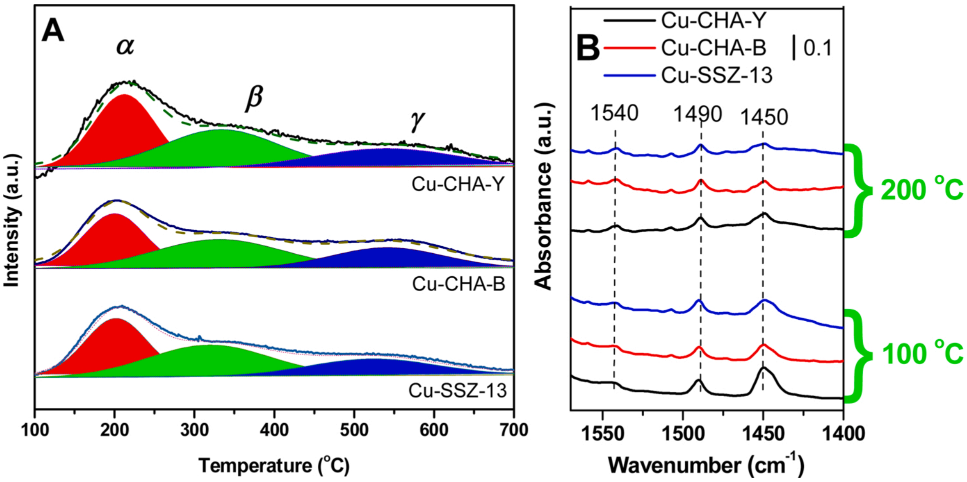

**Fig. 6.** (A) $NH_3$-TPD profiles and (B) Pyridine adsorption IR spectra of Cu−CHA-Y, Cu−CHA-B and the conventional Cu-SSZ-13 catalysts.

molecules, and thereby enhance the $NH_3$-SCR of $NO_x$ reaction.

The pyridine adsorption IR technique was used to determine Brønsted and Lewis acidic sites of catalyst. Exposure of all catalysts to pyridine resulted in the appearance of some weak bands in the 1400 and 1570 $cm^{-1}$ regions as a result of the pyridine molecule (0.6 nm) is bigger than the channel (0.38 nm) of CHA-type zeolite (Fig. 6 **B**). According to previous reports that the bands at around 1452 and 1540 $cm^{-1}$ was assigned to pyridine adsorbed on Cu ions of Cu-exchanged zeolite and Brønsted acid sites on the external surface, respectively. [34] The band at 1490 $cm^{-1}$ is contributed by both Lewis and Brønsted acid sites. [35] It is worth noting that, in all catalysts, the intensity of all peaks shows the maximum value on Cu−CHA-Y (100 or 200 °C), which is closely related to its large external surface. Additionally, this result also proves that the Cu ions are mainly located in the pores of the Cu−CHA-Y (Cu−CHA-B, Cu-SSZ-13) catalyst.

### 3.2.6. $H_2$-TPR analysis of the catalysts

The $H_2$-TPR experiments were conducted to determine the redox behavior of the active Cu sites on catalysts, and the results are shown in **Fig. S8**. Clearly, four $H_2$ consumption peaks were observed during the entire reduction temperature range. The peak at ∼ 190 °C is attributed to the reduction of $[Cu(OH)]^+$-Z species and the $Cu^{2+}$ ion located in the CHA cage balanced by one framework charge [36]. Additionally, the reduction of a small quantity of CuO species is also contributed to the $H_2$ consumption. The peak at ∼ 435 °C is assigned to the reduction of $Cu^{2+}$-2Z species and the isolated $Cu^{2+}$ in the six-membered ring (6MR), balanced by two framework charges [37]. The reduction temperature of $Cu^{2+}$-2Z species is higher than that of $[Cu(OH)]^+$-Z species, demonstrating that the isolated $Cu^{2+}$ in the 6MR is more stable [29]. As reported previously, the $[Cu(OH)]^+$-Z and $Cu^{2+}$-2Z species is produced through a two-step process: $Cu^{2+} + 1/2H_2 \rightarrow Cu^+ + H^+$ and $Cu^+ + 1/2H_2 \rightarrow Cu^\circ + H^+$ [36,37]. The second step is more complex and the reduction temperature is generally above 500 °C. The peaks at about 570 and 766 °C are assigned to the second step reduction of $[Cu(OH)]^+$-Z and $Cu^{2+}$-2Z species, respectively. The UV–vis, EPR and XPS analyses revealed that [Cu(OH)]+-Z and Cu2+-2Z are the dominant species on all catalysts. It is generally accepted that the $[Cu(OH)]^+$-Z and $Cu^{2+}$-2Z species play a key role in the $NH_3$-SCR of $NO_x$ reaction, as they can efficiently convert between $Cu^+$ and $Cu^{2+}$, and then promote the oxidation of reactantsas well as the reduction of intermediate products [38].

### 3.3. $NH_3$-SCR of $NO_x$ performance

The catalytic performance of Cu−CHA-Y, Cu−CHA-B and the conventional Cu-SSZ-13 catalysts in the standard $NH_3$-SCR of $NO_x$ ($4NO + 4NH_3 + O_2 = 4N_2 + 6H_2O$) reaction depends on both the reduction and acidic sites, and these features are closely related to the Cu species and SAR. Moreover, the SAR is also associated with the hydrothermal stability. Compared with the high-silica zeolites, the Al-rich zeolites have an obviously disadvantage in terms of hydrothermal stability. The Al-rich zeolite tends to have more Al in its framework, facilitating an easier dealumination during the hydrothermal aging process. To date, the CHA zeolites with SAR from 6 to 30 have been widely studied, the results of such studies have demonstrated that their framework structure is well maintained preserved during the hydrothermal aging process [14]. Therefore, we believe that it is reasonable to assume that the low-cost Cu−CHA-Y and Cu−CHA-B catalysts prepared in this study have better hydrothermal stability.

All the three catalysts were evaluated for their performance in the $NH_3$-SCR of $NO_x$ reaction and the results are presented in Fig. 7. Fig. 7 **(A)** showing the NO conversion on all catalysts from 100 to 600 °C. All catalysts have essentially similar catalytic performance, and the removal efficiency of NO can reach higher than 98 % in the temperature range from 200 to 450 °C. Compared with the conventional Cu-SSZ-13 catalyst, Cu−CHA-Y and Cu−CHA-B catalysts have slightly good catalytic performance. After hydrothermal aging, Cu−CHA-Y and Cu−CHA-B still exhibited better catalytic performance for NO elimination (Fig. 7 **(A)**), especially Cu−CHA-B, may be due to the larger (1μm) uniform morphology. Additionally, as shown in Fig. 7 **(B)** the $N_2$ selectivity at different temperatures can reach more than 97 % with all the catalysts, indicating that the catalysts also exhibit the lowest secondary pollution (such as $N_2O$).

The kinetic experiments were performed at a high space velocity and low conversions (<15 %) to rule out the external mass transfer and internal diffusion, respectively. All catalysts possess satisfactory activity for $NO_x$ reduction, and the highest 79 % $NO_x$ conversion is achieved at 450 °C under the high space velocity (Fig. 8 **(A)**). The Arrhenius plots for the $NH_3$-SCR of $NO_x$ reaction for the three catalysts are displayed in Fig. 8 **(B).** It should be noted that all catalysts have a similar apparent activation energy, with a value of around 39 kJ $mol^{-1}$, demonstrating that the low-cost catalyst may act through the same $NH_3$-SCR of $NO_x$ mechanism as the conventional Cu-SSZ-13 catalyst [39].

Recently, several studies revealed that the smaller the catalyst crystal particle size, the better its catalytic performance [21,26,39]. Even though the Cu−CHA-Y catalyst has the smallest grains among all

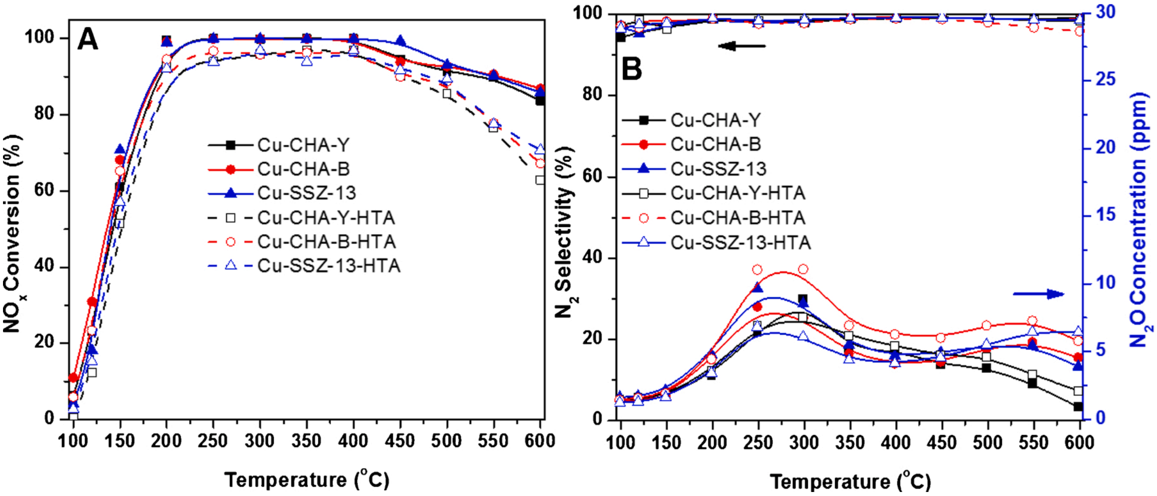

**Fig. 7.** Catalytic performances of catalysts: (A) $NO_x$ conversion; (B) $N_2$ selectivity and $N_2O$ concentration. Reaction conditions: $[NO]=[NH_3] = 500$ ppm, $[O_2] = 5$ vol.%, $N_2$ balance, total flow rate 100 mL $min^{-1}$, 5 vol.% $H_2O$, and GHSV = 48,000 $h^{-1}$.

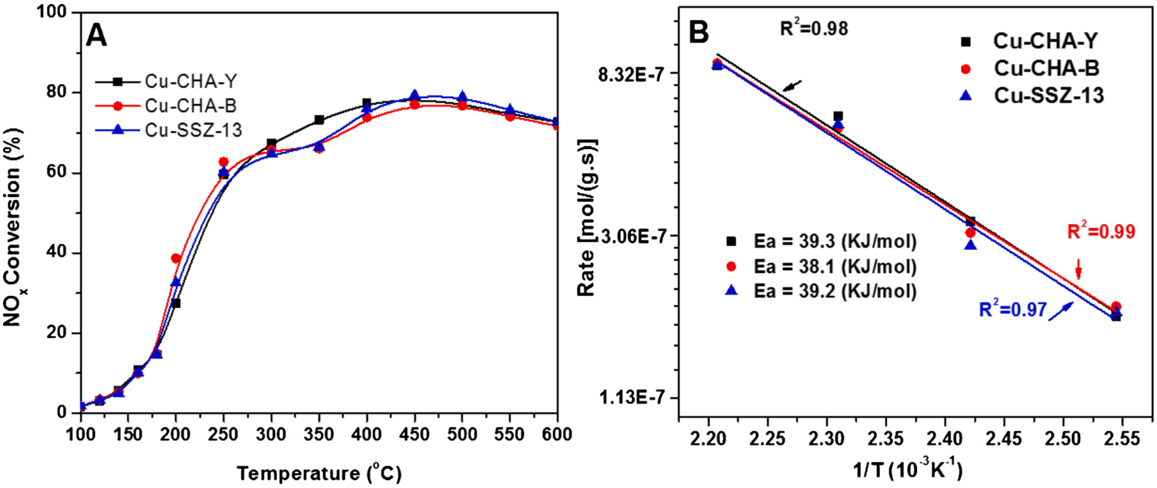

**Fig. 8.** (A) $NO_x$ conversion and (B) Arrhenius plots in $NH_3$-SCR reaction on catalysts. Reaction conditions: [NO] = [$NH_3$] = 500 ppm, [$O_2$] = 5 vol.%, $N_2$ balance, total flow rate 400 mL $min^{-1}$, 5 vol.% $H_2O$, and GHSV = 800,000 $h^{-1}$.

catalysts, it does not have the best catalytic performance in the $NH_3$-SCR of $NO_x$ reaction. This might be due to the existing state of the Cu species. The differences in Cu species have been revealed by UV–vis, EPR and XPS analyses. The Cu−CHA-Y possess relatively fewer isolated $Cu^{2+}$ than the other two catalysts. Considering the key role of $Cu^{2+}$ species in the $NH_3$-SCR of $NO_x$ reaction, it is reasonable to conclude that the Cu−CHA-Y catalyst with smaller crystal particle size has similar catalytic performance as the other catalysts.

In summary, using the inter-zeolite conversion strategy, low-cost effective Cu−CHA-Y and Cu−CHA-B catalysts can be obtained by using CDY-wash-X and H-beta-A as precursors, respectively. The physicochemical properties and catalytic properties of low-cost catalysts are similar to those of the traditional Cu-SSZ-13 catalyst.

### 3.4. *In situ DRIFTS study of the reaction intermediates*

The research of reaction intermediates is of great significance to the development of efficient catalysts. Through the continuous efforts of scientists, the intermediates in the $NH_3$-SCR of $NO_x$ reaction have reached the molecular level. With the aid of DFT calculations, Gao et al. demonstrate that the isolated Cu ions cannot realize the low-temperature oxidation half-cycle of the SCR reaction; $O_2$ activation requires participation of a pair of mobile $[Cu^I(NH_3)_2]^+$ sites with the formation of a $[Cu^I(NH_3)_2]^+$-$O_2$-$[Cu^I(NH_3)_2]^+$ intermediate [40]. At the same time, Gounder. et al. also found the same intermediate in $NH_3$-SCR of $NO_x$ reaction [41]. Recently, Oda. et al. report spectroscopic evidence (fiber-optic UV–vis-NIR spectroscopy) of the efficient generation of the dicopper intermediate($[Cu^I(NH_3)_2]^+$-$O_2$-$[Cu^I(NH_3)_2]^+$) in $NH_3$-SCR over Cu-ion-exchanged zeolites [42]. These findings provide us with very important help in understanding the reaction mechanism. Combined with the conditions of our laboratory, we chose *in situ* DRIFTS technique to understand the reaction intermediates in $NH_3$-SCR of $NO_x$. To our best knowledge, infrared spectroscopy does not have the ability to identify $[Cu^I(NH_3)_2]^+$-$O_2$-$[Cu^I(NH_3)_2]^+$ intermediates. Fortunately, *in situ* DRIFTS technique is sensitive to changes in reactants at the activation site and some intermediate products, such as types of nitrates, $NH_3$ adsorption sites, *etc* [43,44]. Therefore, *in situ* DRIFTS technique is widely used to study the intermediates in $NH_3$-SCR of $NO_x$ reaction. In our study, the *in situ* DRIFTS technique is useful to study the reaction mechanism of the catalyst for a special reaction.

Many studies show that SSZ-13 samples loaded with Cu: Al < 0.2 contain exclusively $Cu^{2+}$ ions isolated in 6-membered ring (6-MR) [45]. Therefore, the Cu ions in our catalyst [Cu−CHA-Y, Cu−CHA-B, Cu-SSZ-13(Cu: Al = 0.16, SAR ≈ 7.8)] are mainly isolated $Cu^{2+}$ ions, as evidenced by UV–vis and EPR results. First, the catalyst was pretreated at 500 °C in $N_2$ for 60 min. Then, the temperature was cooled to the active reaction temperature (200 °C) and subsequently $NH_3$ (500 ppm) was introduced. Eventually, the change of the catalyst surface was monitored by DRIFTS analysis and the results are shown in Fig. 9.

It is worth noting that the bands at about 1430, 1620, 3185, 3282, 3375, 3576, and 3603 $cm^{-1}$ are present in the spectra of all the three catalysts and all the band intensity are increased with increasing exposure time in the $NH_3$ atmosphere. These findings demonstrate that the $NH_3$ species can be adsorbed and activated on the catalyst surface. The characteristics of the catalyst (Cu: Al = 0.16, SAR ≈ 7.8) indicate that the ion exchange of the catalyst is incomplete. Therefore, the IR bands observed after $NH_3$ adsorption represent two distinct ammonia species: the bands at 1430, 3185, 3576, and 3603 $cm^{-1}$ are ascribed to the $NH_4^+$ on the Brønsted acidic sites (Si-O(H)-Al), while the bands at 1620, 3282, and 3375 $cm^{-1}$ are attributed to the coordinated $NH_3$ on the Lewis acidic sites [34,46]. The Lewis acid is dominated by Cu (II), so we speculate the bands are closely related to $[Cu^I(NH_3)_2]^+$ species. Additionally, the band at 1620 $cm^{-1}$ is detected preferentially, indicating that $NH_3$ is more likely to coordinate with Cu (II). It is generally accepted that the bands at high wavenumbers (>3100 $cm^{-1}$) originate from the stretching vibrations of the N—H bonds, and the bands in low wave number region (<1800 $cm^{-1}$) represent the N—H bending vibrations in adsorbed ammonia [46]. Compared with the Cu−CHA-B and Cu-SSZ-13 catalysts, the Cu−CHA-Y catalyst shows the weakest band at 1620 $cm^{-1}$, indicating that the state of the Cu species is the worst, which is well in line with the results of the UV–vis, EPR spectroscopy and XPS analysis. After the $NH_3$ adsorption test, the $NH_3$ was replaced by $N_2$ for 30 min to purge the $NH_3$ of physical adsorption, then 500 ppm NO + 5% $O_2/N_2$ was introduced. Eventually, the spectra were recorded and are presented in **Fig. S9**.

Remarkably, the representative bands at 1430, 1620 and 3282 $cm^{-1}$ began to decrease slowly when 500 ppm of NO + 5% $O_2/N_2$ were introduced, and after 20 min, it was hardly appeared. In 10 min, new bands within the range of ~1550−1650 $cm^{-1}$ emerged, indicating that the activated $NH_3$ species can be reacted with the NO + $O_2$. Noteworthy, the band at around 1620 $cm^{-1}$ is still present, but its position is shifted, indicating that the the coadsorption and interaction of NO and $NH_3$ on a Cu(II) site in Cu−CHA-type led to partial reduction of the site to Cu(I) and the release of $N_2$ and $H_2O$ [43,47].

Additionally, the adsorption and activation of NO on the three catalysts were also studied in detail. First, the catalyst was pretreated at 500 °C in $N_2$ for 60 min. Then, the temperature was cooled to 200 °C. Finally, the mixture of NO (500 ppm) and 5% $O_2/N_2$ was introduced and the

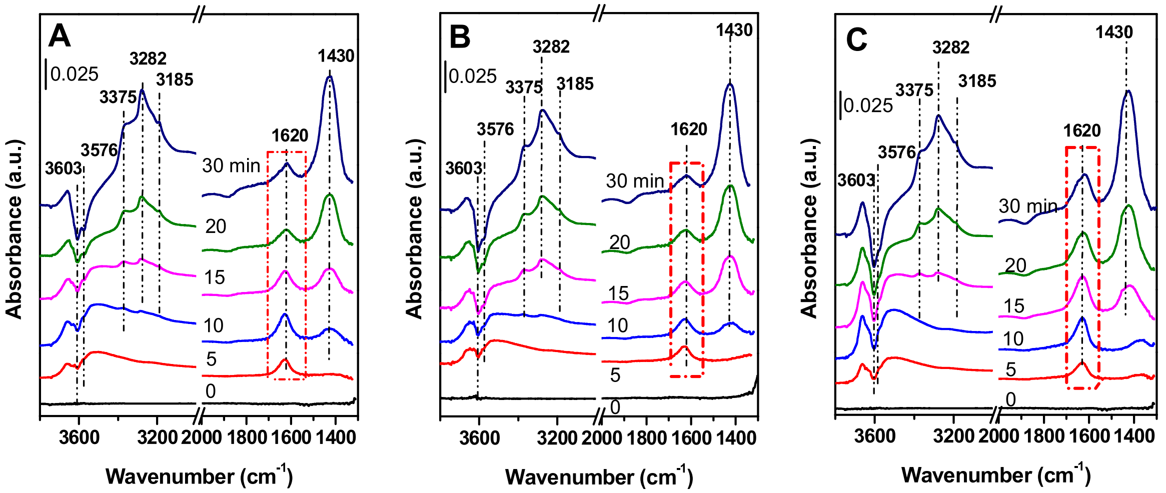

**Fig. 9.** *In situ* DRIFTS spectra of the catalysts under an atmosphere of 500 ppm $NH_3/N_2$ at 200 °C. (A) Cu−CHA-Y, (B) Cu−CHA-B, (C) Cu-SSZ-13.

change on the catalyst surface was monitored by DRIFTS. The obtained spectral profiles shown in Fig. 10 are similar for each catalyst.

Of note, the bands at about 1374, 1438, 1575, 1605, 1623 and 1880 $cm^{-1}$ are present in the spectra of all the three catalysts and all the band intensity are increased with increasing exposure time in the NO + $O_2$ atmosphere. The band at around 1880 $cm^{-1}$ was assigned to NO adsorbed on $Cu^{2+}$ sites [48]. The bands at 1575, 1605, 1623 $cm^{-1}$ were attributed to monodentate nitrate linked to Cu sites, monodentate nitrate linked to Al sites, and bridging nitrate based on Al sites, respectively [43]. Additionally, the peak of the nitrite species ($NO_2$-) was not observed in the spectra as a result of $NO_2$- was very unstable at 200 °C, making it difficult to investigate their reactivity [44].

After introducing 500 ppm of $NH_3/N_2$, the bands attributed to the nitrate species disappeared (**Fig. S10**). At the same time, the bands attributed to the $NH_3$ species are present and the spectrum is similar to that in Fig. 9. These findings showed that the activated nitrate species can be reacted with the $NH_3$. In other words, nitrate was hard to form on the catalyst surface in the presence of $NH_3$ [44,46]. Need to explain here that although the reaction steps based on the IR data of this study can allow us to infer a series of reaction steps that are consistent with our observations, but for the limited amount of data we currently available, it is impossible to present a clear mechanism diagram. Therefore, we can't get detailed reaction steps here, but these steps are similar to previous reports by Li, Gao and Gounder. et al. [40,41,44,49].

## 4. Conclusions

In summary, the low-cost and economic synthesis of Cu−CHA-type catalysts was successfully achieved *via* the inter-zeolite conversion of low-cost high-silica Y zeolites and beta zeolites, respectively. The low-cost synthesized Cu−CHA zeolites possess high crystallinity and excellent *de*$NO_x$ performance compared with the Cu-SSZ-13 catalyst prepared by the conventional expensive method. Importantly, the Cu-CHA-Y and Cu−CHA-B catalysts obtained from the low cost synthesis method also exhibited superior hydrothermal stability (750 °C, 5 vol% $H_2O$, 16 h). The *in situ* DRIFTS results revealed that the reaction intermediates of $NH_3$-SCR of $NO_x$ over the low-cost prepared Cu−CHA catalysts, such as types of nitrates, $NH_3$ adsorption sites, were detected and the Langmuir-Hinshelwood (L-H) mechanism might be occurred. The low-cost synthesis of the small pore CHA-type zeolites developed in this study provide a guidance to reduce the cost of the preparation of *de*$NO_x$ catalysts for commercial application of catalysts like the SSZ-13 zeolites.

## CRediT authorship contribution statement

**Jingyan Zhang:** Conceptualization, Methodology, Experiments, Writing – Original Draft. **Jian Liang and Yangyang Mi:** Experiments and Writing – Original Draft. **Peng Luo, Hao Xu and Mingyuan He:** Writing; Reviewing; Catalyst synthesis supervision. **Honggen Peng:** Supervision, Reviewing, Conceptualization, Writing and Editing. **Peng**

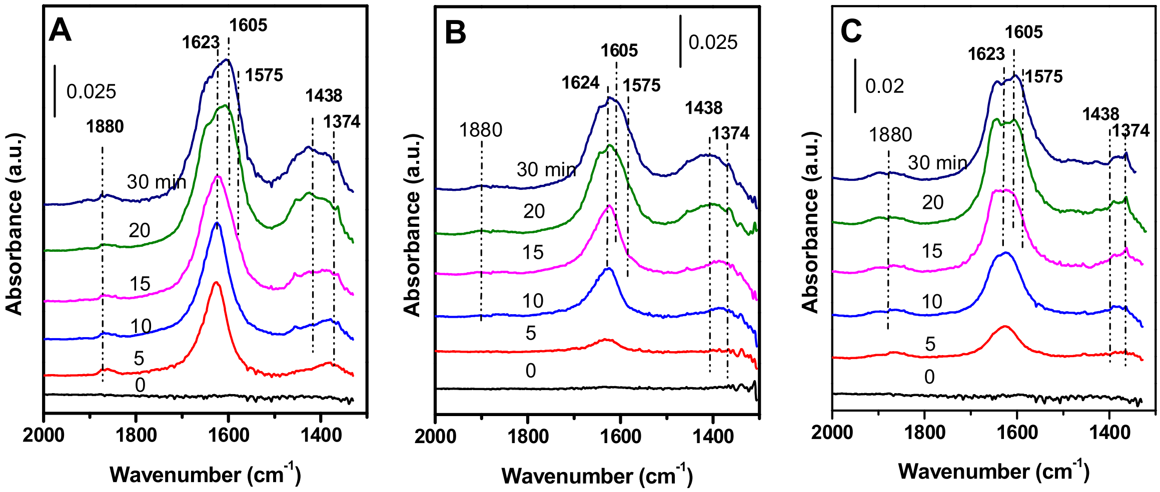

**Fig. 10.** *In situ* DRIFTS spectra of the catalyst under an atmosphere of 500 ppm NO + 5% $O_2/N_2$ at 200 °C. (A) Cu−CHA-Y, (B) Cu−CHA-B, (C) Cu-SSZ-13.

**Wu:** Supervision, Writing – Reviewing and Editing.

## Declaration of Competing Interest

The authors declare that they have no known competing financial interests or personal relationships that could have appeared to influence the work reported in this paper.

## Acknowledgements

This work was supported by the National Natural Science Foundation of China (21872052, 21972044, 21976078 and 21773106), the Ministry of Science and Technology of the People's Republic of China (2016YFA0202804, 2016YFC0205900), National Engineering Laboratory for Mobile Source Emission Control Technology (NELMS2019A12), all of which are greatly acknowledged by the authors.

## Appendix A. Supplementary data

Supplementary material related to this article can be found, in the online version, at doi:https://doi.org/10.1016/j.apcatb.2021.120163.

## References

[1] T. Ryu, H. Kim, S.B. Hong, Nature of active sites in Cu-LTA $NH_3$-SCR catalysts: a comparative study with Cu-SSZ-13, Appl. Catal. B 245 (2019) 513–521.
[2] R. Yu, Z. Zhao, S. Huang, W. Zhang, Cu-SSZ-13 zeolite-metal oxide hybrid catalysts with enhanced $SO_2$-tolerance in the $NH_3$-SCR of $NO_x$, Appl. Catal. B 269 (2020) 118825–118833.
[3] J. Shi, Y. Zhang, Y. Zhu, M. Chen, Z. Zhang, W. Shangguan, Efficient Fe-ZSM-5 catalyst with wide active temperature window for $NH_3$ selective catalytic reduction of NO: synergistic effect of isolated $Fe^{3+}$ and $Fe_2O_3$, J. Catal. 378 (2019) 17–27.
[4] D. Jo, G.T. Park, T. Ryu, S.B. Hong, Economical synthesis of high-silica LTA zeolites: a step forward in developing a new commercial $NH_3$-SCR catalyst, Appl. Catal. B 243 (2019) 212–219.
[5] S. Han, X. Tang, L. Wang, Y. Ma, W. Chen, Q. Wu, L. Zhang, Q. Zhu, X. Meng, A. Zheng, F. Xiao, Potassium-directed sustainable synthesis of new high silica small-pore zeolite with KFI structure (ZJM-7) as an efficient catalyst for $NH_3$-SCR reaction, Appl. Catal. B 281 (2021), 119480.
[6] R. Li, Y. Zhu, Z. Zhang, C. Zhang, G. Fu, X. Yi, Q. Huang, F. Yang, W. Liang, A. Zheng, J. Jiang, Remarkable performance of selective catalytic reduction of $NO_x$ by ammonia over copper-exchanged SSZ-52 catalysts, Appl. Catal. B 283 (2021), 119641.
[7] H. Kubota, C. Liu, T. Toyao, Z. Maeno, M. Ogura, N. Nakazawa, S. Inagaki, Y. Kubota, K. Shimizu, Formation and reactions of $NH_4NO_3$ during transient and steady-state $NH_3$-SCR of $NO_x$ over H-AFX zeolites: spectroscopic and theoretical studies, ACS Catal. 10 (2020) 2334–2344.
[8] D. Jo, T. Ryu, G.T. Park, P.S. Kim, C.H. Kim, I.S. Nam, S.B. Hong, Synthesis of high-silica LTA and UFI zeolites and $NH_3$-SCR performance of their copper-exchanged form, ACS Catal. 6 (2016) 2443–2447.
[9] M. Moliner, C. Franch, E. Palomares, M. Grill, A. Corma, Cu-SSZ-39, an active and hydrothermally stable catalyst for the selective catalytic reduction of NOx, Chem. Commun. 48 (2012) 8264–8266.
[10] Z. Chen, Q. Liu, L. Guo, S. Zhang, L. Pang, Y. Guo, T. Li, The promoting mechanism of in situ Zr doping on the hydrothermal stability of Fe-SSZ-13 catalyst for $NH_3$-SCR reaction, Appl. Catal. B 286 (2021), 119816.
[11] B. Wang, J. Zhang, Y. Ding, H. Peng, H. Xu, Y. Guan, H. Wu, P. Wu, Freestanding cobalt-aluminum oxides on USY zeolite as an efficient catalyst for selective catalytic reduction of NOx, Chem. Cat. Chem. 10 (2018) 4074–4083.
[12] S. Prodinger, M.A. Derewinski, Y. Wang, N.M. Washton, E.D. Walter, J. Szanyi, F. Gao, Y. Wang, C.H.F. Peden, Sub-micron Cu/SSZ-13: Synthesis and application as selective catalytic reduction (SCR) catalysts, Appl. Catal. B 201 (2017) 461–469.
[13] L. Olsson, K. Wijayanti, K. Leistner, A. Kumar, S.Y. Joshi, K. Kamasamudram, N. W. Currier, A. Yezerets, A kinetic model for sulfur poisoning and regeneration of Cu/SSZ-13 used for $NH_3$-SCR, Appl. Catal. B 183 (2016) 394–406.
[14] C. Fan, Z. Chen, L. Pang, S. Ming, X. Zhang, K.B. Albert, P. Liu, H. Chen, T. Li, The influence of Si/Al ratio on the catalytic property and hydrothermal stability of Cu-SSZ-13 catalysts for $NH_3$-SCR, Appl. Catal. A Gen. 550 (2018) 256–265.
[15] F.G.A.M. Beale, I. Lezcano-Gonzalez, C.H.F. Peden, J. Szanyi, Recent advances in automotive catalysis for $NO_x$ emission control by small-pore microporous materials, Chem. Soc. Rev. 44 (2015) 7371–7405.
[16] Y. Guo, T. Sun, X. Liu, Q. Ke, X. Wei, Y. Gu, S. Wang, Cost-effective synthesis of CHA zeolites with controllable morphology and size, Chem. Eng. J. 358 (2019) 331–339.
[17] N.A. Khan, D.K. Yoo, B.N. Bhadra, J.W. Jun, T.W. Kim, C.U. Kim, S.H. Jhung, Preparation of SSZ-13 zeolites from beta zeolite and their application in the conversion of ethylene to propylene, Chem. Eng. J. 377 (2018), 119546.
[18] N. Martin, M. Moliner, A. Corma, High yield synthesis of high-silica chabazite by combining the role of zeolite precursors and tetraethylammonium: SCR of NOx, Chem. Commun. 51 (2015) 9965–9968.
[19] L. Ren, L. Zhu, C. Yang, Y. Chen, Q. Sun, H. Zhang, C. Li, F. Nawaz, X. Meng, F. Xiao, Designed copper-amine complex as an efficient template for one-pot synthesis of Cu-SSZ-13 zeolite with excellent activity for selective catalytic reduction of $NO_x$ by $NH_3$, Chem. Commun. 47 (2011) 9789–9791.
[20] B. Xie, J. Song, L. Ren, Y. Ji, J. Li, F. Xiao, Organotemplate-free and fast route for synthesizing Beta zeolite, Chem. Mater. 20 (2008) 4533–4535.
[21] J. Zhang, F. Liu, J. Liang, H. Yu, W. Liu, X. Wang, H. Peng, P. Wu, Exploring the nanosize effect of mordenite zeolites on their performance in the removal of NOx, Ind. Eng. Chem. Res. 58 (2019) 8625–8635.
[22] Z. Shi, P. Ji, Z. Zhu, J. Jiang, W. Fu, P. Wu, Y. Wang, M. He, Stabilizing low-silica zeolites through aluminum sulfate assisted cannibalistic dealumination, Chem. Cat. Chem. 8 (2016) 1891–1895.
[23] L.S. Dent, J.V. Smith, Crystal structure of chabazite, a molecular sieve, Nature 181 (1958) 1794–1796.
[24] L. Xie, F. Liu, X. Shi, F. Xiao, H. He, Effects of post-treatment method and Na co-cation on the hydrothermal stability of Cu-SSZ-13 catalyst for the selective catalytic reduction of $NO_x$ with $NH_3$, Appl. Catal. B 179 (2015) 206–212.
[25] H. Zhao, Y. Zhao, Y. Ma, X. Yong, M. Wei, H. Chen, C. Zhang, Y. Li, Enhanced hydrothermal stability of a Cu-SSZ-13 catalyst for the selective reduction of $NO_x$ by $NH_3$ synthesized with SAPO-34 micro-crystallite as seed, J. Catal. 377 (2019) 218–223.
[26] J. Liang, Y. Mi, G. Song, H. Peng, Y. Li, R. Yan, W. Liu, Z. Wang, P. Wu, F. Liu, Environmental benign synthesis of Nano-SSZ-13 via FAU trans-crystallization: Enhanced $NH_3$-SCR performance on Cu-SSZ-13 with nano-size effect, J. Hazard. Mater. 398 (2020), 122986.
[27] L. Xie, F. Liu, L. Ren, X. Shi, F. Xiao, H. He, Excellent performance of one-pot synthesized Cu-SSZ-13 catalyst for the selective catalytic reduction of $NO_x$ with $NH_3$, Environ. Sci. Technol. 48 (2014) 566–572.
[28] T. Weissenberger, A.G.F. Machoke, J. Bauer, R. Dotzel, J.L. Casci, M. Hartmann, W. Schwieger, Hierarchical ZSM-5 catalysts: the effect of different intracrystalline pore dimensions on catalyst deactivation behaviour in the MTO reaction, Chem. Cat. Chem. 12 (2020) 2461–2468.
[29] F. Gao, E.D. Walter, E.M. Karp, J. Luo, R.G. Tonkyn, J.H. Kwak, J. Szanyi, C.H. F. Peden, Structure–activity relationships in $NH_3$-SCR over Cu-SSZ-13 as probed by reaction kinetics and EPR studies, J. Catal. 300 (2013) 20–29.
[30] J. Song, Y. Wang, E.D. Walter, N.M. Washton, D. Mei, L. Kovarik, M.H. Engelhard, S. Prodinger, Y. Wang, C.H.F. Peden, F. Gao, Toward rational design of Cu/SSZ-13 selective catalytic reduction catalysts: implications from atomic-level understanding of hydrothermal stability, ACS Catal. (2017) 8214–8227.
[31] R. Moreno-Tost, J. Santamaría-González, E. Rodríguez-Castellón, A. Jiménez-López, M.A. Autié, E. González, M.C. Glacial, C.Dl. Pozas, Selective catalytic reduction of nitric oxide by ammonia over Cu-exchanged Cuban natural zeolites, Appl. Catal. B 50 (2004) 279–288.
[32] B. Pereda-Ayo, U.D.L. Torre, M. Romero-Sáez, A. Aranzabal, J.A. González-Marcos, J.R. González-Velasco, Influence of the washcoat characteristics on $NH_3$-SCR behavior of Cu-zeolite monoliths, Catal. Today 216 (2013) 82–89.
[33] I. Heo, S. Sung, M.B. Park, T.S. Chang, Y.J. Kim, B.K. Cho, S.B. Hong, J.W. Choung, I.S. Nam, Effect of hydrocarbon on $DeNO_x$ performance of selective catalytic reduction by combined reductant over Cu containing zeolite catalysts, ACS Catal. 9 (2019) 9800–9812.
[34] R. Martínez-Franco, M. Moliner, J.R. Thogersen, A. Corma, Efficient one-pot preparation of Cu-SSZ-13 materials using cooperative OSDAs for their catalytic application in the SCR of NOx, Chem. Cat. Chem. 5 (2013) 3316–3323.
[35] S.B.R. Buzzoni, G. Ricchiardi, C. Lamberti, A. Zecchina, Interaction of pyridine with acidic (H-ZSM5, H-β, H-MORD zeolites) and superacidic (H-Nafion membrane) systems: an IR investigation, Langmuir 12 (1996) 930–940.
[36] G. Delahay, B. Cop, L. Broussous, Selective catalytic reduction of nitrogen monoxide by decane on copper-exchanged beta zeolites, Appl. Catal. B 12 (1997) 49–59.
[37] S. Han, J. Cheng, C. Zheng, Q. Ye, S. Cheng, T. Kang, H. Dai, Effect of Si/Al ratio on catalytic performance of hydrothermally aged Cu-SSZ-13 for the $NH_3$-SCR of NO in simulated diesel exhaust, Appl. Surf. Sci. 419 (2017) 382–392.
[38] A.G. Greenaway, A. Marberger, A. Thetford, I. Lezcano-González, M. Agote-Arán, M. Nachtegaal, D. Ferri, O. Kröcher, C.R.A. Catlow, A.M. Beale, Detection of key transient Cu intermediates in SSZ-13 during $NH_3$-SCR $deNO_x$ by modulation excitation IR spectroscopy, Chem. Sci. 11 (2020) 447–455.
[39] T. Yu, J. Wang, M. Shen, W. Li, NH3-SCR over Cu/SAPO-34 catalysts with various acid contents and low Cu loading, Catal. Sci. Technol. 3 (2013) 3234–3241.
[40] F. Gao, D. Mei, Y. Wang, J. Szanyi, C.H. Peden, Selective catalytic reduction over Cu/SSZ-13: linking Homo- and heterogeneous catalysis, J. Am. Chem. Soc. 139 (2017) 4935–4942.
[41] C. Paolucci, I. Khurana, A.A. Parekh, S. Li, A.J. Shih, H. Li, J.R. Di Iorio, J. D. Albarracin-Caballero, A. Yezerets, J.T. Miller, W.N. Delgass, F.H. Ribeiro, W. F. Schneider, R. Gounder, Dynamic multinuclear sites formed by mobilized copper ions in NOx selective catalytic reduction, Science 357 (2017) 898–903.
[42] A. Oda, H. Shionoya, Y. Hotta, T. Takewaki, K. Sawabe, A. Satsuma, Spectroscopic evidence of efficient generation of dicopper intermediate in selective catalytic reduction of NO over Cu-Ion-Exchanged zeolites, ACS Catal. 10 (2020) 12333–12339.
[43] Y. Zhang, Y. Peng, K. Li, S. Liu, J. Chen, J. Li, F. Gao, C.H.F. Peden, Using transient FTIR spectroscopy to probe active sites and reaction intermediates for selective catalytic reduction of NO on Cu/SSZ-13 catalysts, ACS Catal. 9 (2019) 6137–6145.

[44] W. Su, H. Chang, Y. Peng, C. Zhang, J. Li, Reaction pathway investigation on the selective catalytic reduction of NO with $NH_3$ over Cu/SSZ-13 at low temperatures, Environ. Sci. Technol. 49 (2015) 467–473.

[45] C. Paolucci, A.A. Verma, S.A. Bates, V.F. Kispersky, J.T. Miller, R. Gounder, W. N. Delgass, F.H. Ribeiro, W.F. Schneider, Isolation of the copper redox steps in the standard selective catalytic reduction on Cu-SSZ-13, Angew. Chem. Int. Ed. Engl. 53 (2014) 11828–11833.

[46] H. Zhu, J.H. Kwak, C.H.F. Peden, J. Szanyi, In situ DRIFTS-MS studies on the oxidation of adsorbed NH3 by NOx over a Cu-SSZ-13 zeolite, Catal. Today 205 (2013) 16–23.

[47] P. Chen, M. Jabłońska, P. Weide, T. Caumanns, T. Weirich, M. Muhler, R. Moos, R. Palkovits, U. Simon, Formation and effect of $NH_4^+$ intermediates in $NH_3$-SCR over Fe-ZSM-5 zeolite catalysts, ACS Catal. 6 (2016) 7696–7700.

[48] D. Wang, Y. Jangjou, Y. Liu, M.K. Sharma, J. Luo, J. Li, K. Kamasamudram, W. S. Epling, A comparison of hydrothermal aging effects on $NH_3$-SCR of $NO_x$ over Cu-SSZ-13 and Cu-SAPO-34 catalysts, Appl. Catal. B 165 (2015) 438–445.

[49] L. Ma, Y. Cheng, G. Cavataio, R.W. McCabe, L. Fu, J. Li, In situ DRIFTS and temperature-programmed technology study on $NH_3$-SCR of NO over Cu-SSZ-13 and Cu-SAPO-34 catalysts, Appl. Catal. B 156 (2014) 428–437.